Journal of Physics: Photonics

Crossmark

RECEIVED
dd Month yyyy

REVISED
dd Month yyyy

PAPER

Fluorescence Intensity Ratio Analysis of Upconversion Gd_2O_2S: Yb^{3+}, Er^{3+} phosphor for Non-Contact Temperature Sensing

Nabin Chapagain[1,*], Forough Jahanbazi[2], Madhab Pokhrel[1], Yuanbing Mao[2], Amir Shahmoradi[1,3]

[1]Department of Physics, The University of Texas, Arlington, 76010, TX, USA
[2]Department of Chemistry, Illinois Institute of Technology, Chicago, 60616, IL, USA
[3]Division of Data Science, The University of Texas, Arlington, 76010, TX, USA
[*]Author to whom any correspondence should be addressed.

E-mail: nabin.chapagain@mavs.uta.edu

Keywords: Upconversion, Erbium, Fluorescence Intensity Ratio, Thermally Coupled, Optical Thermometry

Abstract
The Fluorescence Intensity Ratio (FIR) of two green emission bands corresponding to the $^2H_{11/2} \rightarrow ^4I_{15/2}$ and $^4S_{3/2} \rightarrow ^4I_{15/2}$ transitions of Er^{3+} in a 9% Yb^{3+},1% Er^{3+} co-doped Gd_2O_2S phosphor is proposed as a model for upconversion-based, non-contact temperature sensing. This phosphor exhibits efficient upconversion luminescence under 980 nm excitation, with the emission intensity of Er^{3+} being strongly temperature dependent—an essential characteristic for ratiometric sensing. The FIR, derived from the ratio of integrated photon counts of the thermally coupled green emission bands which appear in the form of manifolds in nature due to broadening was analyzed as a function of temperature. The Boltzmann-type distribution of these emissions confirms the validity and robustness of the FIR model. The Gd_2O_2S: 9% Yb^{3+}, 1% Er^{3+} phosphor demonstrates high relative thermal sensitivity and resolution, making it a promising candidate for precise, non-contact temperature sensing applications.

1 Introduction

Optical thermometry employing rare-earth ion-doped upconversion (UC) phosphors has emerged as a promising technique for non-contact temperature sensing, particularly in environments where traditional thermometry methods fail due to electromagnetic interference, high temperatures, or small measurement scales. UC phosphors, which convert lower-energy photons (typically near-infrared) into higher-energy emissions (visible or ultraviolet) [1–3], offer unique advantages such as high sensitivity, miniaturization potential, and the ability to measure temperatures with high spatial resolution in biological and industrial applications [4].

Among the rare earth trivalent ions, emissions from Erbium (Er^{3+}) ions are well-suited for optical thermometry [5]. Erbium's electronic states are particularly suitable for luminescence due to several key properties: Erbium (Er^{3+}) has a rich set of energy levels within its 4f electron shell. These levels are shielded by the outer 5s and 5p electrons, which minimize the interaction with the host lattice, leading to sharp optical transitions. This feature results in narrow emission lines with high color purity.

The transitions between the energy levels of Er^{3+}, particularly those from the excited states of $^2H_{11/2}$, $^4S_{3/2}$, and $^4F_{9/2}$ to the ground state ($^4I_{15/2}$), have relatively long lifetimes. This allows for efficient controlling of population density, which is beneficial for applications like temperature sensors because luminescence intensity is a temperature-dependent phenomenon where fluorescence intensity ratio (FIR) changes linearly with temperature [6]. The FIR technique, where the ratio of the intensities of two thermally coupled levels of Er^{3+} (typically $^2H_{11/2}$ and $^4S_{3/2}$) is measured, is commonly employed for temperature sensing. The sensitivity of this method stems from the Boltzmann distribution of the population between these levels, which varies with temperature [7].

The host material compatibility also gives Er^{3+}-doped system a potential advantage as a temperature sensor since Er^{3+} can be doped into various host materials like crystals, glasses, and ceramic powders without significantly altering the luminescence wavelength [8–10]. Due to the crystal field in the host material, the degenerate energy levels of Er^{3+} split into Stark levels, providing more transitions for both absorption and emission, enhancing the versatility in luminescent applications. These characteristics make Er^{3+} a valuable dopant for luminescent materials, where its electronic states can be leveraged to increase the photon yields if doped into a suitable host, as the choice of the host can influence upconversion efficiency.

FIR is typically used to predict the temperature based on the measured intensity because of its higher sensitivity and theoretical linear relationship between the natural logarithm of FIR ($\log(R)$) and the reciprocal of temperature ($1/T$). FIR is defined as the ratio of emissions from higher to that of lower excited levels, which is done by calculating the ratio of integrated intensities for those transitions, which also includes the results of Stark effect [11, 12].

Furthermore, numerous papers discussing optical thermometry have demonstrated the performance of the phosphors up to 550 - 600 Kelvin [13–16]. Finding a host that possesses a low phonon spectral mode while being non-toxic, chemically stable, and can be mass-produced at low cost is a challenge and has garnered a lot of attention recently [9, 17].

Haase et al. [18] identifies $NaYF_4$:Yb/Er as the most efficient host material. However, Pokhrel et al. [19] show that Yb/Er doped Y_2O_2S, La_2O_2S and Gd_2O_2S are equally or even brighter than $NaYF_4$: Yb/Er. Under low power excitation, [19] reports significant upconversion of Yb/Er doped Gd_2O_2S, indicating that the upconversion efficiency in the material is notably higher compared to other materials. This led us to use Yb/Er doped Gd_2O_2S as the host in our experiment, with the doping concentration of 9% Yb^{3+} and 1% Er^{3+} [19]. Further, utilizing this novel phosphor Gd_2O_2S, the luminescence data up to 875 Kelvin was experimentally recorded.

In this work, the temperature-dependent upconversion luminescence data from Gd_2O_2S:9%Yb^{3+}, 1% Er^{3+} phosphor is explored as a more precise, reliable, and versatile temperature sensor, and the challenges and its potential applications for optical thermometry are discussed. By analyzing the spectral changes in upconverted luminescence with temperature, the mechanisms behind the thermal sensing capabilities of this particular dopant and host combination is elucidated. It is demonstrated that Gd_2O_2S: Er,Yb phosphors could be used for high-temperature applications, with sensing capabilities up to at least 875 K.

2 Methodology

2.1 Sample Synthesis

The synthesis of Gd_2O_2S:9%Yb^{3+}, 1%Er^{3+} phosphor was conducted using a solid-state reaction method as described by Kumar et al. (2012) [20]. In this process, stoichiometric amounts of the starting materials, gadolinium oxide (Gd_2O_3), ytterbium oxide (Yb_2O_3), and erbium oxide (Er_2O_3), were thoroughly mixed. Sulfur was added to the mixture as the sulfur source to form the oxysulfide host lattice. The mixture was then subjected to a two-step calcination process. Initially, it was heated in an air atmosphere at a moderate temperature to promote the formation of an intermediate phase. Subsequently, the temperature was increased, and the atmosphere was changed to one with a controlled amount of sulfur vapor to facilitate the conversion of the intermediate to the final Gd_2O_2S phase. The uniformity of the dopant ions, Yb^{3+} and Er^{3+}, was optimized based on the intenisty of the emission under 980 nm wavelength [19]. The detailed conditions and exact temperatures for each step can be found in the cited work [20].

2.2 Measurement and Characterization

To test the optical thermometry potential of the Gd_2O_2S:9%Yb^{3+}, 1%Er^{3+} phosphor, spectroscopic techniques, particularly photoluminescence (PL) spectroscopy were employed, by exciting the phosphor with a 980 nm laser and measured the UC emission spectra at room temperature using an Edinburgh FLS-1000 spectrophotometer. The same spectrometer was used to analyze the luminescence intensity changes as a function of temperature by placing the samples inside a Linkam chamber in which the temperature was controlled by programmable Fluoracle software. To minimize variability in UC measurements, samples were used in powder form, ground using a ball mill, and characterized using an X-ray powder diffractometer (XRD). Specifically, the primary purpose was to identify variations in the ratio of UC emission intensities from distinct electronic transitions of Er^{3+}, which are temperature-sensitive and commonly referred to as the FIR technique. The focus was on the UC luminescence generated from two thermally coupled energy levels and the subsequent non-radiative relaxation process of Er^{3+} dopant.

2.3 Data Analysis

Fluorescence Intensity Ratio (FIR), also known as luminescence intensity ratio, is defined as the ratio of two integrated intensities of two separate manifolds m and n [2, 21],

$$\mathrm{FIR} = \frac{\int_{\lambda_{m,1}}^{\lambda_{m,2}} I \, \mathrm{d}\lambda}{\int_{\lambda_{n,1}}^{\lambda_{n,2}} I \, \mathrm{d}\lambda} \; . \tag{1}$$

An alternative definition relies on the ratio of the peak intensities of two manifolds [22],

$$\mathrm{FIR} = \frac{I_1}{I_2} \; . \tag{2}$$

In this analysis, the photon counts belonging to a manifold, obtained from the FLS1000 spectrometer were utilized rather than just the peak intensities to calculate the ratio. The former FIR definition has an additional complexity level that comes with inferring the unknown wavelength ranges of the manifolds $(\lambda_{m,1}, \lambda_{m,2})$, $(\lambda_{n,1}, \lambda_{n,2})$. A common approach to resolving this challenge is to infer these limits through visual inspection of the manifolds empirically. This approach, while offering a practical venue to define and calculate FIR according to Eqn (1), is subject to uncertainties and biases that manifest as misfits of the resulting FIR-temperature relationship to experimental data.

An alternative, data-driven approach to addressing this issue could involve using mixture modeling to reconstruct the spectrum based on the relevant physics. This would start with identifying the number of peaks in the manifold, which result from Stark splitting of the spectral lines due to the surrounding electric fields in the lattice [23, 24]. The main broadening factors such as inhomogeneous broadening, phonon broadening, that contribute to the continuous spectral line in the manifold could then be identified [25–28]. With this, line profiles corresponding to each peak could be constructed by convolving the broadening functions, and these profiles could be used to fit a mixture model to the available data. However, a comprehensive implementation and application of this data-driven approach is deferred to future work where higher-quality experimental data enables its implementation.

The most straightforward approach to inferring the integration limits involves visually inspecting the line spectra at each temperature [11, 12, 29]. A baseline is identified where no peaks are apparent, and the signal is subtracted from the spectral profile. The corrected dataset is then used for analysis. This approach assumes a constant baseline for the entire spectral profile or, at the very least, for the region of interest used for FIR analysis. Baseline correction is an evolving field of research, as baseline shifts can arise from various factors, including stray light within the spectrometer, dark current flowing in the detector, or scattering of residual excitation light. Various methods have been proposed, such as using the Asymmetric Least-Squares Algorithm [30, 31], which appeared to be overkill for the dataset in question.

Once the baseline correction is applied, the integrated intensities for each spectral profile resulting from their respective emissions could be computed. For spectral profiles that appear as a result of transitions from two thermally coupled energy levels to the ground state, there could be significant overlap between these two separate manifolds. Determining a clear boundary between these two manifolds becomes a difficult yet important task, as is it not desirable to assign one manifold's signal to another. The point in the spectra where the intensity is lowest between the two manifolds for each spectrum is identified and assigned as the boundary between the two manifolds. As for the outer boundaries of the manifolds, they are determined as the wavelength at which the manifolds meet the baseline.

3 Results and Discussion

Figure 1a and 1b shows the crystal structure of Gd_2O_2S, and the XRD pattern of Gd_2O_2S:9%Yb^{3+}, 1%Er^{3+} phosphor, respectively. The symmetry is trigonal, and the space group is P-3m1. There is one formula per unit cell. The structure is very closely related to the A-type rare-earth oxide structure, the difference being that one of the three oxygen sites is occupied by a sulfur atom. Atom positions in Gd_2O_2S using lattice vector units are ± (1/3, 2/3, u) for two metal atoms with u ∼ 0.28, ± (1/3, 2/3, ν) for two oxygen atoms with $\nu \sim 0.63$, and (0, 0, 0) for a sulfur atom. Each metal atom seems to be bonded to four oxygen atoms and three sulfur atoms, to form a seven-coordinated geometry with the oxygen and the metal in the same plane. The XRD results reveal that the well-crystallized Gd_2O_2S: Yb, Er sample is in hexagonal Gd_2O_2S structure with cell parameters a = b = 0.3852 nm, c = 0.6567 nm.

Figure 2a shows the upconversion emission spectrum of Yb^{3+} Er^{3+} co-doped Gd_2O_2S sample in the wavelength range of 250 - 750 nm at 0° to 600° celsius temperature range. The UC spectrum includes peaks at 524 and 549 nm in the green region, and one band centered at 671 nm in the red region. The former is due to the $^2H_{11/2} \rightarrow {}^4I_{15/2}$ and $^4S_{3/2} \rightarrow {}^4I_{15/2}$ transitions, and the latter is due to the $^4F_{9/2} \rightarrow ^4I_{15/2}$ transition. Figure 2b shows a possible upconversion mechanism, in agreement with previous studies [15, 29, 32]. The two energy levels $^2H_{11/2}$ and $^4S_{3/2}$ are thermally coupled. The dominant green lights peaked at 524 and 549 nm, arising due to the $^2H_{11/2} \rightarrow ^4I_{15/2}$ and $^4S_{3/2} \rightarrow ^4I_{15/2}$ transitions, respectively, which result from the efficient two-photon processes that populate the $^4F_{7/2}$ level and a fast multi-photon non-radiative decay of $^4F_{7/2}$ level to $^2H_{11/2}$ level. Because of several closely spaced levels in between $^2H_{11/2}$ and $^4S_{3/2}$, multi-phonon relaxation results in the decay of the $^2H_{11/2}$ level to $^4S_{3/2}$ yielding the strong emission band at 549 nm. A comparatively weak emission is also observed for the 412 nm band (see Figure S1), resulting from $^2H_{9/2} \rightarrow ^4I_{15/2}$ as expected, because the efficiency of the third-order process is less than that of the two-photon process [19, 20].

Inferring temperature from the available fluorescence intensity is a complex task. The fluorescence intensity from a specific energy level of an ensemble of ions doped in a host material is influenced by various parameters, including the host material, the energy level of interest, the dimensions of the material doped with the ion, and the excitation method employed. By measuring the intensity of fluorescence originating from a specific energy level, the temperature can be theoretically inferred by observing temperature dependent changes in fluorescence intensity. These changes are usually influenced by various non-radiative rates, such as increased phonon interactions and multi-phonon relaxation, which depend directly on temperature. The intensity of each transition is proportional to the number of atoms (population) in a given excited state at temperature T [2, 6]:

$$I_{1\rightarrow 2} \propto gAh\nu \exp\left(-\frac{E}{K_B T}\right) \tag{3}$$

where, g is the degeneracy of the state, A is the spontaneous emission rate, ν is the frequency, E is the energy of the level, and h and k_B are the Planck constant and Boltzmann constant respectively. The primary challenge associated with employing a single intensity is that any alterations in the excitation intensity, whether attributable to variations in excitation power or excitation wavelength, would be erroneously interpreted as changes in temperature. To circumvent this issue, a method can be employed that involves measuring the intensity of fluorescence from two distinct energy levels that exhibit varying temperature dependencies [33, 34]. This approach provides a self-referencing quantity as a measurand, thereby ensuring that the calibration of the thermometer is entirely independent of the host matrix. This new quantity is defined as Fluorescence Intensity Ratio (FIR). As defined in Eq (1), FIR can be rewritten as follows:

$$\mathrm{FIR} = \frac{\int_{\lambda_{m,1}}^{\lambda_{m,2}} I \; \mathrm{d}\lambda}{\int_{\lambda_{n,1}}^{\lambda_{n,2}} I \; \mathrm{d}\lambda} = \frac{g_1 A_1 h\nu_1}{g_2 A_2 h\nu_2} \exp\left(-\frac{\Delta E_{12}}{K_B T}\right) = B \exp\left(-\frac{\Delta E_{12}}{K_B T}\right) \tag{4}$$

where B is a constant, subscripts 1 and 2 being two distinct energy levels, and ΔE is the energy difference between the two thermally linked levels. The ratio ν_1/ν_2 is absorbed into B as they are the frequencies for theoretical transition emission, or the peak of the distribution, which will stay relatively the same even when the temperature changes. Even though energy levels may undergo a slight shift with a temperature change, for the purposes of this paper,it is assumed they remain constant.

The FIR model appears to work best when calculating the ratios of two closely spaced energy levels, often referred to as "thermally coupled" energy levels [35]. Two energy levels are said to be in thermal equilibrium if the separation of energy levels is in the order of a 1-10 kT, where kT $\sim$ 200 cm^{-1} [2, 36]. The ratio of emission intensities from these energy levels can be understood using the concept of Boltzmann's thermal equilibrium. These empirical limits ensure that the spectral separation is sufficient and the distance is not excessive, thereby allowing for a small exponential temperature decay rate (determined by ΔE). This was proven by our analysis, as shown in Figure 3a. For the analysis, the ratios of integrated intensities were computed for each combination of observed manifolds and examined the relationship between the natural logarithm of the fluorescence intensity ratios (FIR) and the inverse temperature. A linear dependence in these plots would indicate a Boltzmann-type behavior of the intensity ratios.

Upconversion processes based on energy transfer, which involve optical pumping, might not seem to follow the Boltzmann distribution at first glance, as it appears that the optical pumping directly influences the population of Stark levels in Er^{3+}. Yet, it can be seen in Figure 3a that there exists a Boltzmannian relationship for thermally coupled energy levels. For thermally coupled energy levels, due to such a small energy gap, phonon-mediated thermalization occurs in picoseconds whereas the upconversion pumping from Yb^{3+} and radiative decay from the Er^{3+}

sublevels occur much slowly in the range of microseconds [19, 37]. As the non-radiative multiphonon transition rates between the coupled excited states are substantially higher than the radiative and other competitive relaxation rates, it can be assumed the distribution followed by thermally coupled energy levels is indeed Boltzmannian in nature, as it is in a steady state [38].

For the analysis, the ratio of integrated intensities of two thermally equilibrated manifolds were chosen with respective emission intensity peaks at 524 nm and 549 nm. The ΔE for these two energy levels is $\sim$ 870 cm^{-1}. Figure 3b shows the total integrated intensities for each manifold of emission for Er^{3+} ion in the range of 250 - 750 nm, set in log scale. The bold plots show the change in emission intensity resulting from thermally coupled energy levels, thanks to the phonon contribution between these two energy levels. Even though equation (3) clearly says the intensity has to go down with increasing temperature, it can be seen that the total photon count for the 524 nm peak actually increases slowly, while the total photon count for the 549 nm peak actually decreases rapidly. This increment in the photon count of the 524 nm peak can be attributed to non-radiative phonon-based energy transfer from the manifold with a peak at 549 nm to the manifold with a peak at 524 nm. Interestingly, the total photon counts for 496 nm peaks, even though they are only in thousands, also increase with increasing temperature, almost mimicking the 524 nm curve. An in-depth investigation of this phenomenon is deferred to later publications.

The ratio in Equation (4) can be written as

$$\log \mathrm{FIR} = \log \mathrm{B} + \left(\frac{-\Delta E_{12}}{k_B} \right) * \frac{1}{\mathrm{T}} \tag{5}$$

The experimental data are fitted to a straight line with a slope of -1277.6198 and an intercept of 2.3947. The relationship between FIR and temperature can be represented using these values, $\log \mathrm{FIR} = 2.3947 - 1277.6198/\mathrm{T}$. The dependence of FIR on temperature in the range of 0° to 600° celsius is shown in Figure 4a and 4b.

The absolute thermal sensitivity indicates how the FIR model responds to changes in temperature. It can be defined as follows:

$$\mathrm{S}_a = \frac{\partial \mathrm{FIR}}{\partial \mathrm{T}} = \mathrm{B} \left(\frac{\Delta \mathrm{E}}{k_B \mathrm{T}^2} \right) \exp \left(\frac{-\Delta \mathrm{E}}{k_B \mathrm{T}} \right) \tag{6}$$

The sensor sensitivity (S_a) for our model is illustrated in Figure 4c. As it can be seen from the graph, the absolute sensitivity reached the maximum of 0.00464 K^{-1} at the temperature of 648.15 K (375°) celcius. In addition, another measure of sensitivity known as relative thermal sensitivity is utilized, denoted as S_r. S_a is unsuitable for comparing the performance of dissimilar luminescent thermometers because it is influenced by sample characteristics (such as absorption and lifetimes) and the experimental setup. The relative thermal sensitivity S_r, often expressed in units of % change per Kelvin of temperature change (%K^{-1}) or as fractional change per unit of Kelvin (K^{-1}), quantifies the relative change in FIR per degree of temperature change and offers a significant advantage by being independent of the thermometer's nature [2, 39]. It is defined as follows:

$$\mathrm{S}_r = \frac{1}{\mathrm{FIR}} \left| \frac{\partial \mathrm{FIR}}{\partial \mathrm{T}} \right| = \left| \frac{\Delta \mathrm{E}}{k_B \mathrm{T}^2} \right| = \frac{1277.6198}{\mathrm{T}^2} \tag{7}$$

Figure 4d shows the change in relative sensitivity with change in temperature. The Equation (7) is multiplied by 100 % if the preferred unit is percentage change per Kelvin. The maximum relative thermal sensitivity was found to be 0.01712 K^{-1} at 0° C (273.15 K).

Thermometer	**Temp. Range** (K)	λ_{ex} (nm)	$-\Delta$ **E/k**$_\mathbf{B}$ (K)	**Sa** (10^{-3} K)	**Sr** $^{\mathbf{max}}$ (% K^{-1})	δT (K)	**Ref.**
Gd_2O_2S: 9%Yb, 1%Er	273-873	980	1277.62	4.64 (648 K)	1.71	0.35 (300 K)	This work
Er: Oxyfluoride Glass	293-720	488	773/k_B	6.6 (570 K)	-	-	[40]
$GdVO_4$: 2%Er, 8%Yb	300-453	375	1212.79	11.04 (450 K)	1.34	0.37 (300 K)	[41]
$GdVO_4$: 1%Er, 20%Yb	300-453	980	1107.19	12.56 (453 K)	1.20	0.41 (303 K)	[41]
$NaYbF_4$: 1%Er	175-475	980	1059.69	-	3.46	-	[42]
Gd_2O_3: 1%Er, 10%Yb	298-578	980	1028	640 (298 K)	1.28	-	[43]
$CaMoO_4$: 0.5%Er, 8 %Yb	303-873	980	733/k$_B$	14.3 (575 K)	-	-	[44]

Table 1: Thermometric parameters (thermal sensitivities and temperature uncertainties) of several FIR-based luminescent thermometers utilizing Er^{3+}-doped and Er^{3+}, Yb^{3+} co-doped hosts. The temperatures in parentheses indicate the values at which the parameters in this table are computed. The Boltzmann constant is $k_B = 0.6950348\,\mathrm{cm}^{-1}\mathrm{K}^{-1}$.

Temperature resolution (also referred to as temperature uncertainty) δT is the smallest temperature change that the luminescent thermometer can detect. A thermometer with high resolution (low uncertainty) is considered to be best for temperature sensors applications [14]. It can be calculated using equation (8)

$$\delta \mathrm{T} = \frac{1}{S_r} \frac{\delta \mathrm{FIR}}{\mathrm{FIR}} \tag{8}$$

where δFIR/FIR is the sensitivity of the detection system. For the PMT device, the sensitivity of the detection system is 0.03 % at maximum singal to noise ratio (SNR) operating conditions, but it is advised to use 0.5 % in general scenario [2]. Figure 4e represents the thermal sensitivity in general and maximum SNR condition, where the minimum uncertainty is 1.7520 % K (0.01752 K) at 273.15 K, and the maximum uncertainty is 17.9018 % K (0.1790 K) at 873.15 K for maximum SNR condition. In a general condition, the minimum and maximum uncertainties were found to be 0.29199 K and 2.9836 K, respectively. As evident by the equations [(5), (7)], the pairs of energy levels with larger energy difference (ΔE) result in larger FIR and sensitivity. The optical thermometry performance of different hosts doped with Erbium ions have been presented in the Table 1 in the decreasing order of the energy difference obtained as a result of the data fitting. $GdVO_4$:2%Er, 8%Yb phosphor was reported with S_r value of 1.34 $\%K^{-1}$ and temperature uncertainty of 0.37 K under excitation at 375 nm while $GdVO_4$:1%Er, 20%Yb counterpart showed slightly worse temperature uncertainty and S_r values under excitation at 980 nm [41]. Our Gd_2O_2S:Yb^{3+}, Er^{3+} phosphor performed better than these counterparts reported in the literature with higher S_r and lower thermal uncertainty δT while in wider temperature range. The performance of our host can be attributed to higher upconversion quantum yield for metal oxysulfide phosphors even at lower power densities compared to other hosts such as β-$NaYF_4$:Er,Yb [19]. Also, the higher range of temperature for the emisison intensity measurement played significant role in improving the accuracy of the prediction of ΔE of thermally coupled energy levels (see Figure S2).

4 Conclusions

In this study, we have demonstrated the Gd_2O_2S : 9% Yb^{3+}, 1% Er^{3+} upconversion phosphors as a potential candidate for optical thermometry, leveraging Er^{3+} temperature-dependent luminescence properties for non-contact based temperature sensing. Through detailed spectral analysis, we proposed the mechanisms governing the thermal sensitivity of this phosphor, particularly the FIR of the thermally coupled ${}^2H_{11/2} \rightarrow {}^4I_{15/2}$ and ${}^4S_{3/2} \rightarrow {}^4I_{15/2}$ transitions of Er^{3+} under 980 nm excitation. Our results confirm that Gd_2O_2S : Er, Yb phosphors exhibit exceptional thermal sensing capabilities, with reliable performance up to 875 K, making them suitable for high-temperature applications in harsh environments where conventional sensors are impractical. Our findings show the potential of Gd_2O_2S: 9% Yb^{3+}, 1% Er^{3+} phosphors for applications in different areas such as industrial monitoring, aerospace, and biomedical diagnostics, where high sensitivity and non-invasive sensing are essential. Our work lays the groundwork for the development of next-generation optical thermometers, combining advanced materials with data-driven approaches to address the demands of emerging technological challenges. These results can be further improved with higher-resolution data, enabling the development of a completely data-driven FIR model minimally affected by uncertainties and biases due to human intervention (e.g., visual inspections) in the FIR model construction.

Supplementary information

Supplementary Information is available from the journal/author.

Conflict of interest

The authors have no conflicts to disclose.

Data availability

The data that support the findings of this study are available upon reasonable request from the corresponding author.

Acknowledgments

YM would like to thank the financial support of the IIT startup funds.

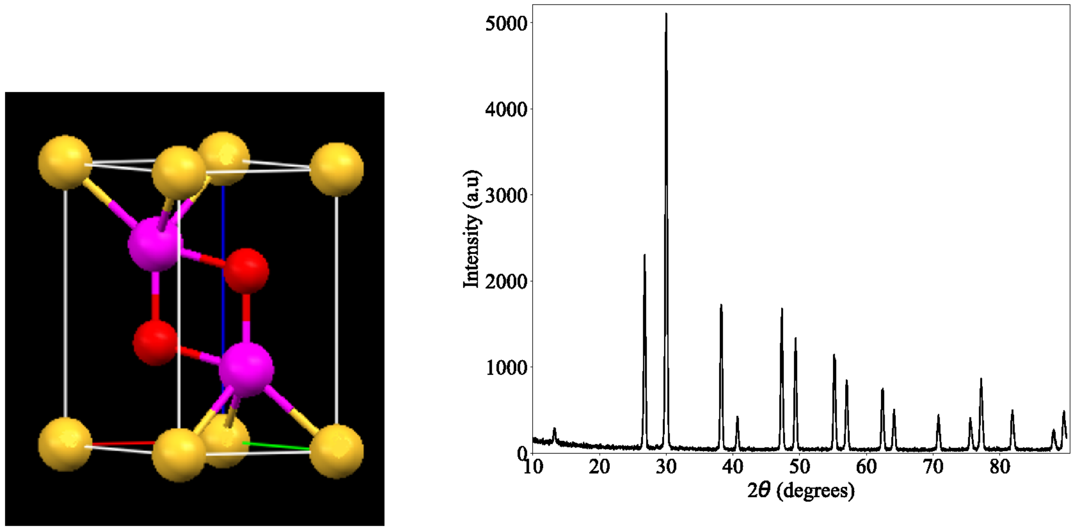

(a) (b)

Figure 1: (a) Crystal structure of Gd_2O_2S, illustrating the arrangement of constituent atoms within the unit cell. (b) X-ray diffraction (XRD) pattern of Gd_2O_2S:9%Yb^{3+}, 1%Er^{3+} where intensity is measured in arbitrary units (a.u.) and θ is the angle of diffraction, confirming the phase purity and crystallographic structure of the synthesized sample, agreeing the space group is P-3m1.

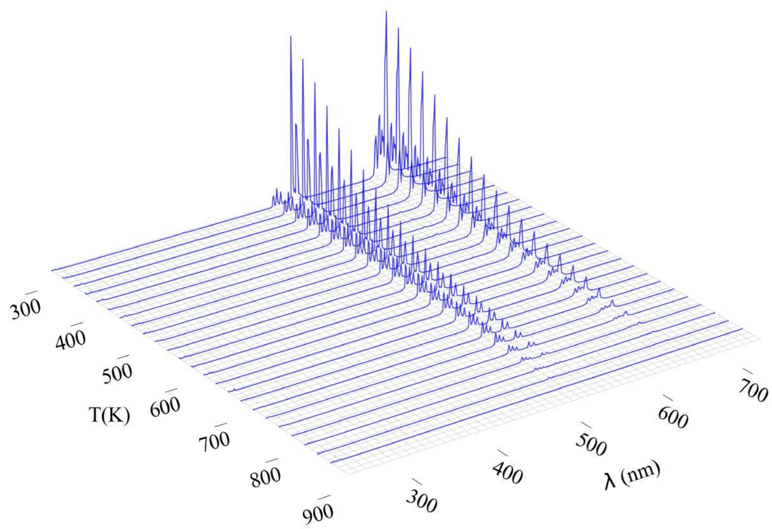

(a)

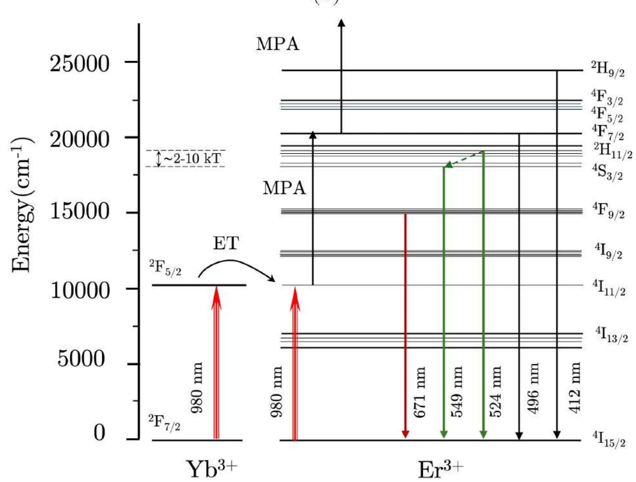

(b)

Figure 2: (a) Temperature-dependent emission spectra of Gd_2O_2S:9%Yb^{3+}, 1%Er^{3+} presented as a 3D plot, showing variation in photon counts as a function of wavelength (nm) and temperature (K). (b) Proposed energy level diagram of Er^{3+} ions, depicting the radiative transitions responsible for the observed emission and absorption spectra [5].

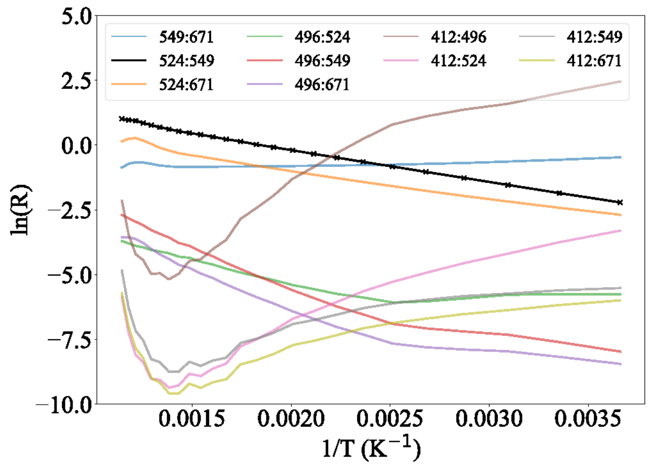

(a)

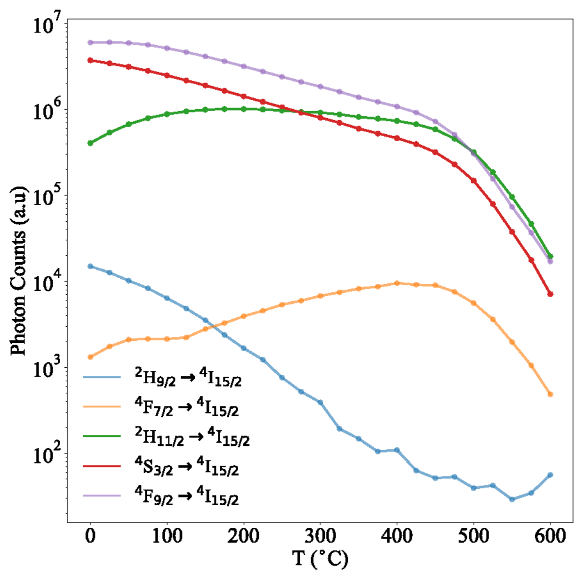

(b)

Figure 3: (a) Plot of the natural logarithm of the fluorescence intensity ratio (FIR) versus the reciprocal of the absolute temperature (1/T) for various pairs of emission transitions. Each curve represents the FIR between two distinct transitions, with the legend indicating the peak emission wavelengths. The observed linear behavior reflects the Boltzmann distribution characteristic of thermally coupled energy levels. (b) Temperature dependence of the integrated UC emission intensities of various transitions of the Gd_2O_2S:9%Yb^{3+}, 1%Er^{3+}. Integrated photon counts are plotted as a function of temperature (°C), with individual transitions indicated in the legend.

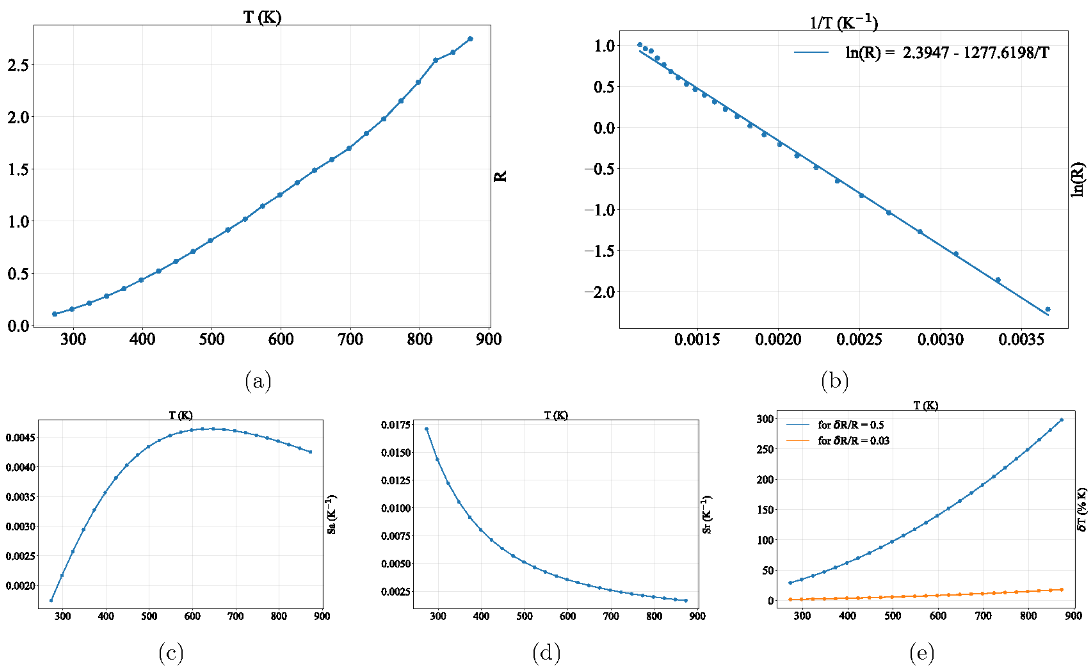

Figure 4: Thermal sensing performance of Gd_2O_2S analyzed through multiple optical thermometry metrics: (a) FIR as a function of temperature (K), showing the variation in emission behavior with thermal input; (b) natural logarithm of FIR plotted against the reciprocal of absolute temperature (K^{-1}), with a linear fit applied to extract temperature-dependent characteristics; (c) absolute sensitivity (K^{-1}) versus temperature(K), illustrating the material's responsiveness to temperature changes; (d) relative sensitivity (K^{-1}) versus temperature(K), indicating the fractional response per unit temperature; and (e) temperature uncertainty (%K) as a function of temperature, with two trendlines corresponding to different analysis methods, as labeled.

References

[1] Phillips M L, Hehlen M P, Nguyen K, Sheldon J M and Cockroft N J 2000 Upconversion phosphors: recent advances and new applications *Physics and Chemistry of Luminescent Materials: Proceedings of the Eighth International Symposium* vol 99 No, 40 (The Electrochemical Society) p 123

[2] Brites C, Millán A and Carlos L 2016 Lanthanides in luminescent thermometry *Handbook on the physics and chemistry of rare earths* vol 49 (Elsevier) pp 339–427

[3] Ong L C, Gnanasammandhan M K, Nagarajan S and Zhang Y 2010 *Luminescence* **25** 290–293

[4] Jahanbazi F and Mao Y 2021 *Journal of Materials Chemistry C* **9** 16410–16439

[5] Pokhrel M, Sardar D K *et al.* 2013 *Materials letters*

[6] Brites C D, Balabhadra S and Carlos L D 2019 *Advanced Optical Materials* **7** 1801239

[7] Li T, Guo C, Zhou S, Duan C and Yin M 2015 *Journal of the American Ceramic Society* **98** 2812–2816

[8] Pokhrel M, Gupta S K, Perez A, Modak B, Modak P, Lewis L A and Mao Y 2021 *ACS Applied Nano Materials* **4** 13562–13572

[9] Wang X, Cao Y, Mao Y, Liu T, Yan X, Li L, Zhang J and Chen B 2024 *Inorganic Chemistry* **63** 1439–1448

[10] Zhang Y, Hao J, Mak C L and Wei X 2011 *Optics express* **19** 1824–1829

[11] Abbas M, Khan N, Mao J, Qiu L, Wei X, Chen Y and Khan S 2022 *Materials Today Chemistry* **24** 100903

[12] Elzbieciak-Piecka K and Marciniak L 2022 *Scientific reports* **12** 16364

[13] Hou B, Jia M, Li P, Liu G, Sun Z and Fu Z 2019 *Inorganic Chemistry* **58** 7939–7946

[14] Jahanbazi F, Wang Y, Dorman J A and Mao Y 2022 *Journal of Alloys and Compounds* **911** 165013

[15] Yang Y, Mi C, Yu F, Su X, Guo C, Li G, Zhang J, Liu L, Liu Y and Li X 2014 *Ceramics International* **40** 9875–9880

[16] Zhou S, Deng K, Wei X, Jiang G, Duan C, Chen Y and Yin M 2013 *Optics Communications* **291** 138–142

[17] Wang X, Jahanbazi F, Wei J, Segre C U, Chen W and Mao Y 2022 *ACS Applied Materials & Interfaces* **14** 36834–36844

[18] Haase M and Schäfer H 2011 *Angewandte Chemie International Edition* **50** 5808–5829

[19] Pokhrel M, Kumar G and Sardar D 2013 *Journal of Materials Chemistry A* **1** 11595–11606

[20] Kumar G, Pokhrel M, Martinez A, Dennis R, Villegas I and Sardar D 2012 *Journal of Alloys and Compounds* **513** 559–565

[21] Kusama H, Sovers O J and Yoshioka T 1976 *Japanese Journal of Applied Physics* **15** 2349

[22] Morita K, Katsumata T, Komuro S and Aizawa H 2014 *Review of Scientific Instruments* **85**

[23] Jha A, Shen S and Naftaly M 2000 *Physical Review B* **62** 6215

[24] Sangwan V, Jayasimhadri M and Haranath D 2024 *Journal of Physics D: Applied Physics* **57** 195301

[25] Demtröder W 1973 *Laser spectroscopy* vol 2 (Springer)

[26] Bernath P F 2020 *Spectra of atoms and molecules* (Oxford university press)

[27] Fox M 2010 *Optical properties of solids* vol 3 (Oxford university press)

[28] Gornushkin I B, King L A, Smith B W, Omenetto N and Winefordner J D 1999 *Spectrochimica Acta Part B: Atomic Spectroscopy* **54** 1207–1217

[29] Balabhadra S, Debasu M L, Brites C D, Ferreira R A and Carlos L D 2017 *The Journal of Physical Chemistry C* **121** 13962–13968

[30] He S, Zhang W, Liu L, Huang Y, He J, Xie W, Wu P and Du C 2014 *Analytical Methods* **6** 4402–4407

[31] Dong Z y and Xu J l 2024 *Measurement* **233** 114731

[32] Xu W, Gao X, Zheng L, Wang P, Zhang Z and Cao W 2012 *Applied physics express* **5** 072201

[33] Zhao Y, Bai G, Hua Y, Yang Q, Chen L and Xu S 2020 *Journal of Luminescence* **221** 117037

[34] Zhang H, Ye J, Wang X, Zhao S, Lei R, Huang L and Xu S 2019 *Journal of Materials Chemistry C* **7** 15269–15275

[35] Wade S A 1999 *Temperature measurement using rare earth doped fibre fluorescence* Ph.D. thesis Victoria University

[36] Wade S A, Collins S F and Baxter G W 2003 *Journal of Applied physics* **94** 4743–4756

[37] Van Hest J J, Blab G A, Gerritsen H C, de Mello Donega C and Meijerink A 2018 *The Journal of Physical Chemistry C* **122** 3985–3993

[38] Suta M and Meijerink A 2020 *Advanced Theory and Simulations* **3** 2000176

[39] Yang X, Fu Z, Yang Y, Zhang C, Wu Z and Sheng T 2015 *Journal of the American Ceramic Society* **98** 2595–2600

[40] León-Luis S F, Rodríguez-Mendoza U R, Haro-González P, Martín I R and Lavín V 2012 *Sensors and Actuators B: Chemical* **174** 176–186

[41] Bhiri N M, Dammak M, Aguilo M, Diaz F, Carvajal J J and Pujol M 2020 *Journal of Alloys and Compounds* **814** 152197

[42] Baziulyte-Paulaviciene D, Karabanovas V, Stasys M, Jarockyte G, Poderys V, Sakirzanovas S and Rotomskis R 2017 *Beilstein journal of nanotechnology* **8** 1815–1824

[43] Zheng W, Sun B, Li Y and Wang R 2021 *ACS Applied Nano Materials* **4** 3922–3931

[44] Huang F, Gao Y, Zhou J, Xu J and Wang Y 2015 *Journal of Alloys and Compounds* **639** 325–329